An Externally Dispersed Interferometer for Sensitive Doppler Extrasolar Planet Searches

JIAN GE,[1] DAVID J. ERSKINE, AND MIKE RUSHFORD

Lawrence Livermore National Laboratory, Livermore, CA 94550; erskine1@llnl.gov

ABSTRACT. A new kind of instrument for sensitive Doppler extrasolar planet searches, called an externally dispersed interferometer, is described in this paper. It is a combination of an optical Michelson-type interferometer and an intermediate-resolution grating spectrometer. The interferometer measures Doppler radial velocity (RV) variations of starlight through the phase shifts of moiré fringes, created by multiplication of the interferometer fringes with stellar absorption lines. The intermediate-resolution spectrograph disperses the moiré fringes into thousands of parallel-wavelength channels. This increases the instrument bandwidth and fringe visibility by preventing fringe cross-talk between neighboring spectral lines. This results in a net increase in the signal-to-noise ratio over an interferometer used alone with broadband light.

Compared to current echelle spectrometers for extrasolar planet searches, this instrument offers two unique instrument properties: a simple, stable, well-defined sinusoidal instrument response function (point-spread function) and magnification of Doppler motion through moiré fringe techniques. Since instrument noise is chiefly limited by the ability to characterize the instrument response, this new technique provides unprecedented low instrumental noise in an economical compact apparatus, enabling higher precision for Doppler RV measurements. In practice, the moiré magnification can be 5–10 times depending on the interferometer comb angle. This instrument has better sensitivity for smaller Doppler shifts than echelle spectrometers. The instrument can be designed with much lower spectral resolving power without losing Doppler sensitivity and optimized for higher throughput than echelle spectrometers to allow a potential survey for planets around fainter stars than current magnitude limits.

Lab-based experiments with a prototype instrument with a spectral resolution of $R \approx 20,000$ demonstrated ~ 0.7 m s^{-1} precision for short-term RV measurements. A fiber-fed version of the prototype with $R \approx 5600$ was tested with starlight at the Lick 1 m telescope and demonstrated ~ 7 m s^{-1} RV precision at 340 Å bandwidth. The increased velocity noise is attributed to the lower spectral resolution, lower fringe visibility, and uncontrolled instrument environment.

1. INTRODUCTION

Currently, there are over 80 known extrasolar planets orbiting nearby stars (Vogt et al. 2000; Fischer et al. 2001 and references therein). The discovery of these planets has captured the imagination of both astronomers and the general public. From a scientific perspective, the diversity of these planetary systems has challenged conventional theories of planet formation, providing insight into the processes that may have shaped our own solar system.

All of the planets discovered using precision Doppler radial velocity (RV) measurements (e.g., Marcy & Butler 1998; Marcy, Cochran, & Mayor 2000) are through optical spectroscopy with cross-dispersed echelle spectrometers (e.g., Mayor & Queloz 1995; Marcy & Butler 1996; Noyes et al. 1997; Cochran et al. 1997). Almost all of them have been discovered around F, G, and K type stars. The demonstrated long-term RV accuracy approaches 3 m s^{-1} (Butler et al. 1996; Vogt et al. 2000). Minimum masses of known extrasolar planets range upward from 0.16 M_J with semimajor axes extending out to 3 AU (Marcy, Butler, & Vogt 2000; Mayor et al. 2000). An important new class of planets has been defined, which have roughly Jovian mass but orbital periods of only a few days. Recent models of planetary formation suggest that these planets may have migrated toward the star from larger orbits, sweeping away any terrestrial planets (Lin, Bodenheimer, & Richardson 1996), perhaps affecting the frequency of habitable planets. In any case, the search for planets with lower mass and larger orbital radii remains intrinsically interesting, and these will have smaller velocity signatures. Also, the search for long-period (multiyear) planets will inevitably involve observations over less than a full orbit. These will benefit from increased velocity precision, particularly if their signature needs to be separated from larger signals of other companion bodies.

RV precision is limited by a combination of factors: instru-

---

[1] Current address: Department of Astronomy and Astrophysics, Penn State University, University Park, PA 16802; jian@astro.psu.edu.

ment noise, photon noise, intrinsic stellar photosphere activity induced noise, wavelength calibration errors, and CCD inhomogeneity induced error (see Butler et al. 1996 for detailed discussions). Instrument noise is essentially determined by the ability to measure the point-spread function (PSF) in effect at the moment of observation with sufficient precision. The PSF can wander with time as a result of environmental factors. Since a 1 m s^{-1} precision is approximately 5000 times smaller than the width of typical stellar absorption lines, exceedingly small changes in the centroid of the PSF become important. Therefore, it is crucial to have a stable and precise instrument response over a long time interval for precision RV measurements.

The photon noise can be reduced by improving instrument total throughput and increasing the telescope photon collection power. High-throughput instruments on large ground-based telescopes would potentially allow better RV precision and enable observations of fainter objects to allow surveys of thousands of stars for planets. The intrinsic photospheric activity induced noise can be potentially reduced through modeling stellar activity in the data analysis and frequent observation to separate more stochastic activity from the strictly periodic RV signal. Recent analysis of Lick echelle spectra by Saar et al. demonstrates that most stars appear to have some magnetism related radial velocity noise at the level of at least a few meters per second (Saar, Butler, & Marcy 1998). This kind of noise can be modeled and partially removed from the net velocity signal at some level with simultaneous measurements of high-precision radial velocities and magnetic activity (S. H. Saar 1999, private communication; Saar & Fischer 2000).

The uncertainty in the PSFs of current cross-dispersed echelle spectrometers causes an RV measurement error of ~2 m s^{-1} (Butler et al. 1996; Vogt et al. 2000). Further improvement is extremely difficult. Fundamentally, the PSF of an echelle is very complicated (Valenti, Butler, & Marcy 1995). This is because it is formed by the interference among thousands of grating grooves, and any changes in grating optical properties, aberration, and illumination could affect the resulting PSF, which would introduce errors in the RV measurements.

1.1. Externally Dispersed Interferometer Approach

A new approach based on an externally dispersed interferometer (EDI, previously referred to as a fringing spectrometer; Erskine & Ge 2000), can significantly reduce the instrument noise to allow 1 m s^{-1} or better precision for Doppler RV measurements. This instrument is a combination of an undispersed wide-angle Michelson-type interferometer with a fixed delay and an external intermediate-resolution grating spectrometer. Similar approaches based on wide-field interferometers with fixed path differences operating in a narrow band have been actively used in high-precision RV measurements in solar astrophysics since the 1980s (Title & Ramsey 1980; Harvey et al. 1995; Kozhevatov, Kulikova, & Cheragin 1995, 1996). The best RV precision of ~3 m s^{-1} has been reported with a

single Fe I line at 5576.2 Å at the solar disk center. The new feature we add to this instrument is the external intermediate-resolution grating spectrometer for separating fringes from different wavelengths. Nevertheless, our approach is significantly different from previous proposed holographic heterodyning spectroscopy (HHS) for high-precision stellar RV measurements based on a variable delay interferometer (e.g., Douglas 1997; Frandsen, Douglas, & Butcher 1993): in this approach, one or both interferometer mirrors are replaced by a grating to generate rapidly varying optical path difference without moving parts. The resulting interference patterns from different delays are recorded by a detector array and Fourier transformed to a narrowband high-resolution spectrum. These kinds of instruments are modified Fourier transform spectrographs (FTSs) without scanning, and, in principle, they can be used for high-precision RV measurements since the PSFs are better defined and more stable than the echelle spectrometers. However, their sensitivity is less than grating spectrometers because of the small-wavelength bandwidths (≤30 Å) and the superposition of fringes from different wavelengths (high background noise). The latter hurdle was overcome by using a postdisperser (Frandsen et al. 1993). However, the former is the fundamental limit. In current echelles, ~1000 Å wavelength coverage is used for reducing photon noise in RV measurements (e.g., Butler et al. 1996). This results in ~6 times higher Doppler precision for echelles than these previous kinds of heterodyned instruments for the same spectral resolution.

In our approach, the bandwidth is limited only by the total detector size at the spectrometer and not by the interferometer itself. This is because our interferometer contains no significantly dispersive elements internal to its cavity, so the path lengths through the interferometer to the point of interference are, ideally, independent of wavelength. Thus, the fringe visibility can be uniformly high and with uniform frequency response over a very wide bandwidth. Let the optical path length difference between the two arms be called the delay (τ) in units of cm. Then the transmission frequency response $T(\nu)$ of one output arm of an idealized interferometer is

$$T(\nu) = \frac{1}{2}[1 + \cos(2\pi\tau\nu)], \qquad (1)$$

where frequency ($\nu = 1/\lambda$) is conveniently in units of wavenumbers (cm^{-1}). The density of fringes in frequency space is proportional to τ, which, other than a slight wavelength dependence to the glass delay plate that contributes to τ, is fixed over an extremely wide bandwidth. Hence, $T(\nu)$, also called the spectral comb, can have extremely wide bandwidth limited only by the transmission/reflection capabilities of the beam splitter and other transparent elements. Hence, typically the bandwidth-limiting element of the net EDI instrument is not the interferometer but the external grating spectrometer/CCD detector.

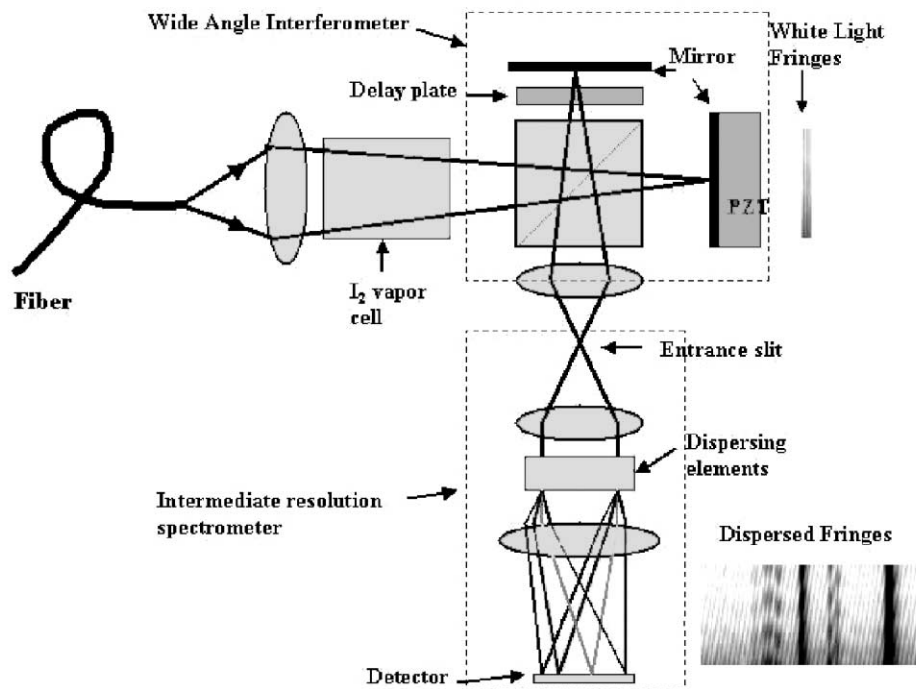In addition to producing fringes in frequency space, the in-

Fɪɢ. 1.—Schematic layout of an externally dispersed interferometer. The light from a fiber from the telescope leads to an iodine vapor cell, which provides wavelength calibration. The incoming beam is split into two beams with equal amplitude by a beam splitter in a Michelson-type interferometer. A parallel glass plate with a 6.3 mm thickness is located in one of the interferometer arms to create 11 mm fixed optical delay between the two beams. A virtual white-light fringe pattern is created at the mirror plane of the interferometer arm that is without the delay plate. The virtual white fringe pattern, reimaged onto the entrance slit of the spectrometer, is dispersed by a dispersing element (a moderate-resolution grating). The dispersed fringes are recorded on a detector.

terferometer with a fixed delay, along with a slight tilt in an internal mirror, creates fringes spatially (transverse to the dispersion direction of the grating spectrometer). These have a spatial period proportional to λ. Over moderate bandwidths, this is a relatively slow change.

In contrast, in the HHS technique, the fringe period in the spatial direction is proportional to $1/(\lambda - \lambda_0)$, where λ_0 is set by the alignment of a grating internal to the interferometer (e.g., Douglas 1997). While this divergent behavior provides high spectral resolution in the neighborhood of λ_0, the operational bandwidth is relatively small because outside this range the spatial period becomes too fine to be cleanly resolved by the CCD pixels in the transverse direction.

Hence, in the EDI technique, the relatively uniform behavior of the interferometer fringes (both spatially and vs. frequency) is over a bandwidth similar to that of the echelles. The simple and stable sinusoidal instrument responses provided by the interferometer have only 3 significant degrees of freedom (phase, amplitude, and vertical offset). This is in contrast with the many more of degrees of freedom (on the order of the number of grating grooves) with an echelle response. The smaller number of degrees of freedom can lead to less systematic error than

the echelle and can simultaneously cover broad wavelengths to reduce errors due to photon statistics.

Because of this, different calibration sources can potentially be used for observing at other wavelengths. This opens up new possibilities for searching for extrasolar planets around late M type dwarfs in the near-IR where the peak flux and major absorption lines are. It could also possibly be used for observing early-type stars and white dwarfs in the near-UV where strong Balmer series lines exist.

Figure 1 shows a schematic drawing of the instrument. A fiber-fed telescope beam is divided equally into two beams by a beam splitter in the interferometer. Virtual white-light interference fringes (the interferogram) are formed on the interferometer mirror plane and imaged onto the spectrometer entrance slit plane. After these white fringes pass through the spectrometer, the fringes from different wavelengths are separated from each other by a dispersing element (such as a moderate-resolution diffraction grating) and reimaged onto a CCD array to create a two-dimensional fringing spectrum. This fringing spectrum can also be interpreted as multiplication of a stellar spectrum with an interferometer comb, as shown in Figure 2. The fringe density in the slit spatial direction (or cross-
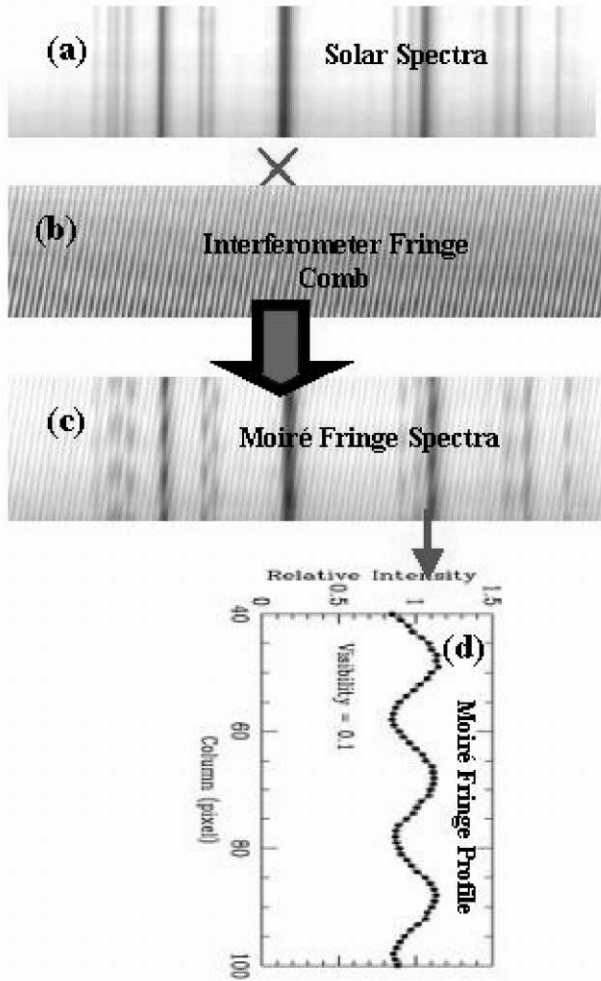
FIG. 2.—Formation of moiré fringes in a solar spectrum: multiplication of (*a*) a pure solar spectrum with (*b*) an interferometer comb produces (*c*) a moiré fringing spectrum. The response of the moiré fringing spectrum in slit direction is (*d*) a truncated sinusoidal function.

dispersing direction, or vertical direction in the figure) and orientation at each frequency are adjusted by the tip and tilts of the mirrors.

In our approach, instead of using a grating to measure the Doppler shift $\Delta\lambda$ or $\Delta\nu$ of a spectrum, we use an interferometer to measure the corresponding shift in fringe phase $\Delta\phi$ for every stellar absorption line (or other spectral feature). The external grating just serves to separate neighboring spectral lines from each other to improve the net fringe visibility. Since neighboring features have randomly related fringe phase, without external dispersion the net fringe visibility for all the wavelengths combined at the detector is extremely low (hence, the low photon signal-to-noise ratio [S/N] of FTSs).

To calculate the change in phase $\Delta\phi$ (in radians) due to a Doppler wavelength shift $\Delta\lambda$ at a given position in the spectrum

(given λ), it is helpful to consider the number (N) of wavelengths that fit "inside" the delay:

$$N = \frac{\tau}{\lambda}. \tag{2}$$

For our interferometer, where $\tau \approx 11$ mm and $\lambda \approx 5400$ Å, $N \approx 20{,}000$. Hence, a 1 part in 20,000 fractional change in λ due to a Doppler shift would create one whole fringe (2π of $\Delta\phi$) of phase shift. Since $c/20{,}000 \approx 15$ km s^{-1}, we have a velocity per fringe proportionality of VPF ~ 15 km s^{-1} per revolution (or cycle, or wave) of fringe phase.

For nonrelativistic target velocities, the Doppler-shifted wavelength is

$$\lambda = \lambda_0 + \Delta\lambda \approx \lambda_0\left(1 + \frac{v}{c}\right), \tag{3}$$

where v is the velocity of the source, c is the speed of light, and λ_0 is the original wavelength. Hence, the shift is very small in relative terms, and we can approximate

$$\Delta\lambda = \lambda\frac{v}{c}. \tag{4}$$

For simplicity, let us ignore the minor wavelength dependence of the refractive index in the glass delay plate. Then, taking the derivative $dN/d\lambda$ leads us to

$$\Delta N = -\frac{\tau}{\lambda^2}\Delta\lambda = -\frac{\tau}{\lambda}\frac{v}{c}. \tag{5}$$

Then the velocity is determined from the phase shift $\Delta\phi$ through

$$v = -c\frac{\lambda}{\tau}\Delta N = -c\frac{\lambda}{\tau}\frac{\Delta\phi}{2\pi}. \tag{6}$$

Considering the glass refractive index dispersion could change the delay by a few percent (Barker & Schuler 1974). A way to measure the effective value for τ that automatically includes refractive index dispersion in the operating interferometer is to observe a spectral comb and plot the fringe number versus frequency. Then

$$\tau = \frac{N_2 - N_1}{\nu_2 - \nu_1}. \tag{7}$$

The fringes are made slanted by tilting one of the interferometer mirrors so that the delay has a linear component along the *y*-direction (transverse to the dispersion direction, along the slit):

$$\tau = \tau_0 + \lambda \frac{y}{P_y}, \tag{8}$$

which produces a spatially dependent linear phase shift increment

$$\Delta\phi = 2\pi \frac{y}{P_y}, \tag{9}$$

where P_y is the spatial period of the fringe along the y-direction. Then, shifts in phase will make the entire fringing spectrum appear to shift in the y-direction, transverse to the dispersion direction. Correspondingly, the Doppler velocity shift is found from the transverse shift by

$$v = c \frac{\Delta y}{P_y} \frac{\lambda}{\tau}. \tag{10}$$

In our design, one fringe is usually sampled by ~4 pixels in the dispersion direction, while it is represented by $P_y \sim 20$ pixels in the spatial direction. Therefore, Doppler shifts causing one fringe shift, or 4 pixel shift, in the dispersion direction can cause 20 pixel shift in the spatial direction. This conversion of fringe motion, which we call moiré magnification, facilitates measurements of Doppler shifts.

For a typical BK7 glass parallel plate with ~6.3 mm thickness in the interferometer, the total optical delay is ~11 mm at 5400 Å. For this delay, ~1 m s^{-1} Doppler shift creates ~1/15,000 moiré fringe phase shift in waves. For typical solar spectra obtained at Lawrence Livermore National Laboratory (LLNL), S/N = 200 per pixel, moiré fringe visibility equal to 0.13, and 80 pixels sampling of the moiré fringes, the phase measurement accuracy per wavelength channel is about 1/2000 wave. Therefore, to reach ~1 m s^{-1} precision, about 60 wavelength channels having spectral features are required. A more accurate analysis of the photon S/N would parallel the analysis done by Connes (1985) for a conventional Doppler spectrometer, where the quality factor Q of the spectrum is computed through an rms of the spectrum's derivative.

The interferometer is chosen to be a wide-angle design so that the delay is independent of input ray angle. This produces the best fringe visibility for extended sources such as optical fibers, spectral lamps, or blurry star images and removes errors in alignment of the interferometer relative to the source from affecting the velocity result. The angle-independent condition is achieved by superposing the virtual image of one mirror, as seen behind the glass delay plate, longitudinally with the mirror of the other arm (Hilliard & Shepherd 1966). This way, according to ray paths, the interferometer appears to have zero path length difference and hence is angle-independent. Yet there is a nonzero temporal delay, and this creates the desired frequency behavior $T(\nu)$.

The delay is then caused by both displacement of the mirror position and the slower time of flight $d(\eta - 1)$ through the glass of thickness d and refractive index η. One is free to set the mirror displacement to any value, and hence the delay can be any value. However, the mirror position that generates the optimum visibility is when the superposing condition described above is satisfied, which is when the displacement is $d(\eta - 1)/\eta$, plus or minus a tolerance that decreases with increasing numerical aperture of the beam. Under those conditions the total round-trip delay, which is the sum of the two components, is given by

$$\tau = 2d\left(\eta - \frac{1}{\eta}\right). \tag{11}$$

Because of the operational uncertainty in the mirror position that produces the best fringe visibility, this equation should be used only as an estimate of what the delay could be. The spectroscopic method of determining delay value described above is more accurate.

In the setup shown in Figure 1, a slightly converging beam is used to feed the interferometer instead of a collimated beam to minimize the area of the beam that intersects the beam splitter, which has some wave front error, to maximize fringe visibility. The reimaging lens after the interferometer can be a regular achromat or a cylindrical lens. An achromat was used in our lab testing at LLNL, and the cylindrical lens could be used to collapse a circular fringe image to a line image for increasing spectrometer slit transmission. During the first-light observations at the Lick 1 m telescope, we slightly modified this design and put the cylindrical lens before the interferometer. Details are described in § 2.2.

Because all wavelengths travel the same optical path through the interferometer, the spectroscopic behavior is extremely regular with frequency, since it is a sinusoid with only 3 degrees of freedom—phase, amplitude, and offset—and has a periodicity in frequency space that is constant over the bandwidth (determined by the delay). Many environmental factors that would affect the PSF of a grating do not change the functional character of the interferometer response. For example, a hypothetical change in the reflectivity of an internal mirror surface due to corrosion or condensation will alter the phase, amplitude, or offset of the sinusoid, but the response will remain a sinusoid. This allows the data analysis to be robust against many kinds of drifts.

As a result of the moiré magnification of the Doppler signal, typically 5–10 times, a spectrometer with much lower spectral resolving power than current echelle spectrometers can be used for measuring radial velocity without losing Doppler sensitivity. Lower spectral resolution enables a much more compact, inexpensive, and high-throughput design of instrument for extrasolar planet searches.

When taking data using the slanted fringe as described here,

the spectrometer needs two-dimensional spectra with enough space in the slit direction for superposing the interferometer comb. This requires optics such as integral field units or cylindrical optics to change the image shape from a circular one to a rectangular one. The cylindrical optics may be placed before or after the interferometer, and we have experimented with both arrangements. Use of a cylindrical lens does not change the periodicity of the interference pattern.

Initial tests with the prototype EDI on bright sources including sunlight, bromine absorption cell, and bright stars ($V = 0$–1) confirm that the fundamental velocimetry aspect of the new optical technique works and can reach ~1 m s^{-1} short-term instrument noise using off-the-shelf components. In this paper, we report a description of the instrument (§ 2), instrument performance (§ 3), and discussions (§ 4). The data-taking procedure and data-reduction algorithms will be published in a follow-up paper (Erskine & Ge 2002).

2. IMPLEMENTATION OF AN EDI

2.1. A Prototype for Lab Experiments

The EDI lab prototype instrument was proposed and assembled by one of the authors (Erskine) during 1997–1998 using commercially available optics and a CCD camera with 2500×600 pixels and 12×24 μm pixel size from Princeton Instrument, Inc. Part of the technical aspects about this prototype is described in previous publications (Erskine & Ge 2000; Erskine 2001). Many similar techniques can also be found in previous other literature (e.g., Title & Ramsey 1980; Frandsen et al. 1993; Harvey et al. 1995; Kozhevatov et al. 1995, 1996; Douglas 1997). A commercial spectrograph of Jobin-Yvon HR640 type (Czerny-Turner type) and a Michelson-type interferometer were used in this prototype. An iodine absorption cell was used for providing instrument calibration. The temperature of the cell was controlled to 50°C $\pm$ 0.1°C.

The whole instrument was mounted on an optical bench in a lab at LLNL. The setup is similar to the schematic drawing shown in Figure 1. A fused silica fiber with 1 mm diameter was used to input light from emission line and continuum lamps, HeNe lasers, and solar light. The fiber-fed incoming beams were split by a 50/50 BK7 beam-splitting cube. One beam was delayed by a BK7 plate with a 6.3 mm thickness, corresponding to a total optical delay of 11.3 mm. The output interferometer fringe orientation and density were adjusted by the tip/tilt of the interferometer mirrors. The fringe orientation for a single frequency source such as an HeNe 0.6328 μm laser was kept in the horizontal direction. The spatial fringe density was adjusted to the desired value, which was typically four to six fringes across the beam at the slit. A piezoelectric (PZT) pusher was attached to one mirror to provide piston motion for stepping the delay by quarter-wave increments in several exposures. This phase stepping is used to isolate actual fringes from spurious intensity variations, such as CCD pixel gain variations, which could be confused as fringes. The common

mode errors are distinguished from the true fringes by the lack of proper phase variation with PZT dither.

The interferometer and spectrograph were operated at f/8. The image size at the spectrograph entrance was about 2.0 mm in diameter. An adjustable slit was used for the experiments. A 70 μm width was set for most of the lab testing to provide a spectral resolution of $R \approx 20,000$ with a 1200 line mm^{-1} grating operated in the second dispersion order at 5400 Å. The full-wavelength coverage with the CCD detector was about 124 Å. Figure 2 shows typical fringing spectra taken with this prototype.

This prototype was used for the lab experiments until 1999 April, when we modified the instrument for observing at the Lick 1 m telescope. Some preliminary results from this prototype were reported in a previous conference proceedings (Erskine & Ge 2000).

2.2. A Fiber-fed Instrument for Starlight Testings

The fiber-fed dispersed interferometer was modified from the lab prototype. The modifications involved (1) adding cylindrical optics to convert the round telescope output beams to rectangular cross-sections to more efficiently fit the beams through the slit, (2) construction of a fiber optic feed to couple with telescope Cassegrain focus, (3) active stabilization of the interferometer cavity to allow long time exposures coordinated with phase stepping, and (4) reassembly of the prototype on a small breadboard that can be easily relocated to the observatory.

Fiber feeding was chosen to easily couple the instrument with the telescope. It allows the instrument be located at a convenient place for the testing. It also improves the instrument stability by separating the instrument from the telescope.

The optical layout was designed with a commercial ray-tracing software, ZEMAX (Focus Software, Inc.). The subsystems include a fiber feed, an interferometer, and a spectrograph. The fiber-feed layout at the telescope Cassegrain focus and its schematic drawing are shown in Figure 3. It includes a field lens located at the telescope Cassegrain focus to form an image of the telescope exit pupil. A reimaging lens changes the telescope f/17 beam to f/20. A pinhole with a reflecting aluminum surface was placed at the new image plane. The surface reflects the light to a commercial Cohu CCD camera for finding and guiding the target stars within the 40″ field of view. The f/20 beam was converted to f/4 by a small achromat and then inserted into a fiber with a 70 μm diameter, corresponding to 3″.6 on the sky.

The instrument was bench mounted on an optical table shown in Figure 4. A schematic drawing of the optical layout is also shown. It was placed in the Lick 1 m telescope dome during our first-light observations at Lick Observatory. The interferometer subsystem includes a beam splitter with a BK7 glass parallel plate, a fiber output coupler, a cylindrical lens, a field lens, and a reimaging lens. The beam splitter was the same one used in the lab version. The field lens keeps the pupil
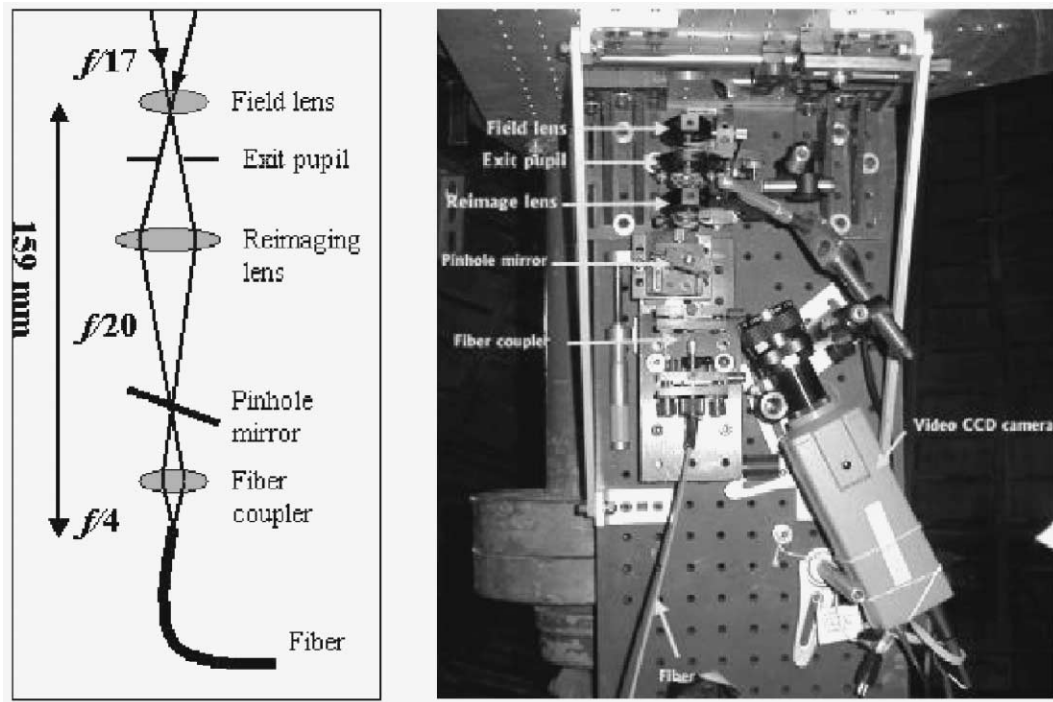
FIG. 3.—Optomechanical structure and schematic drawing of the fiber feed at the Lick 1 m Cassegrain focal plane in 1999 December.

within the aperture of the reimaging lens. The fiber feeds the instrument at f/4 and the input image diameter is 70 μm. The line image produced by the cylindrical lens had a size of about 1.2 × 11 mm on the interferometer mirrors. The superposition of the two line images over each other forms a fringing image. By adjusting the tip and tilt of the interferometer mirrors, the fringe orientation and density were set to the desired values. The fringe is reimaged to the spectrograph entrance slit plane by a field lens and a reimaging lens. The size of the fringe

image at the entrance slit plane is about 140 × 2000 μm at f/8 because of etendue (or $A\Omega$) constancy. This image plane is conjugate to the interferometer mirror planes and is also conjugate to the CCD detector plane. The use of the cylindrical lens over the former spherical does not change the periodicity of the underlying interferometer transmission pattern. It serves just to increase the amount of flux backlighting such fringes.

The same spectrograph housing as the prototype was used for the experiments but with a different choice of grating. To
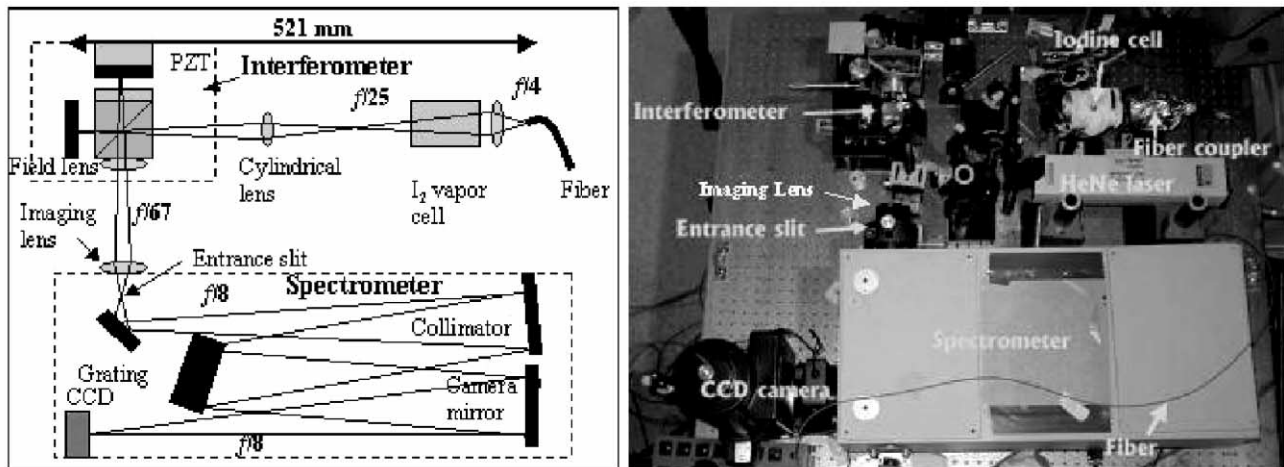

FIG. 4.—Setup and schematic drawing of the instrument on an optical bench in the Lick 1 m telescope dome in 1999 December.

increase the instrument throughput for observing stars, the 1200 line mm^{-1} grating was operated in the first-order configuration instead of the second order used in the lab. Consequently, the resulting spectral resolution was reduced from its prior $R \approx 20,000$ value to $R \approx 5600$ at 5400 Å for a projected slit width of 84 μm (or 7 pixels) on the detector. The whole CCD covered 340 Å in this single order. At this lower resolution, the spectrometer could not resolve the underlying interferometer fringe comb, resulting in more cross-talk between adjacent channels of the remaining moiré fringes. The visibility of the moiré fringes decreases as the slit width increases. This is caused by the convolution of the original high-contrast moiré with the wide slit window function in the dispersion direction. However, the fringe position in the slit spatial direction, which determines Doppler shifts, is not affected by this convolution (or wide-slit blurring).

The alignment of the fiber feed at the telescope was typically conducted in the following procedure: the telescope pupil was aligned to the exit pupil, then the location of the pinhole was adjusted until the image filled it. An HeNe laser beam was directed backward from the instrument bench to align the fiber end with the pinhole and the exit pupil.

2.3. An Interferometer Cavity Control System

A single-channel closed-loop electronic system was constructed to stabilize and control the interferometer delay to prevent the interferometer from drifting significantly over long (multiminute) time exposures. At the Lick 1 m telescope, the interferometer delay was found to wander significantly over both the short term (~1 minute) and long term (>10 minutes) as a result of changing temperature and pressure in the telescope dome. For instance, long timescale variations caused the delay to advance approximately 40 waves over several hours. In order to preserve integrated fringe visibility, the delay must not wander more than ~λ/8 during the exposure. The tilt of the mirror also drifted during long exposures, which diminishes fringe visibility. Unfortunately, tilt was not corrected by the stabilization scheme, although that could be done in the future.

In our cavity control system, a 632.8 nm HeNe laser beam was used as the probe to pass through the interferometer, adjacent to the starlight beam, to trace phase variations. This beam generated a fringe ladder of about four waves that was recorded by a TV-CCD camera. This image was sent to a dedicated computer that actuated the PZT piston motion using a closed-loop feedback algorithm written in LabView software (National Instruments, Inc.).

Note that it is not necessary to stabilize the cavity to high precision (λ/15,000) to reach high-velocity precision (1 m s^{-1}), because small drifts in τ affect both the stellar and the iodine (reference) fringing spectra similarly, and the velocity is a differential result. Rather, the stabilization is to prevent macroscopic drifts (>λ/8). In fact, the high-precision data of Figure 5 (stationary bromine tests) were obtained with the cavity unstabil-
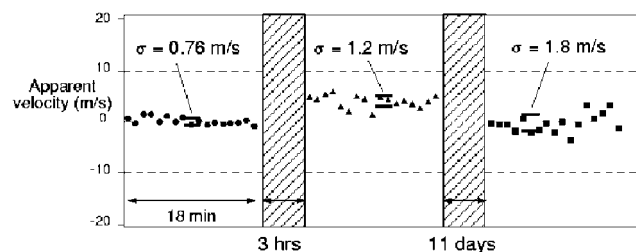

FIG. 5.—Zero-velocity repeatability provided by the prototype instrument at LLNL. Bromine absorption is used to simulate a zero-velocity Doppler source for the measurement. Disperser resolution $R = 20,000$.

ized and sometimes wandering as much as ~λ/8 during the 15 s exposures.

3. PERFORMANCE OF THE EDI

Experiments with the prototype were conducted at LLNL and the Lick 1 m telescope to test its performance. The performance shows very promising results at both sites but also shows several areas where technical improvement is needed for the future instruments.

3.1. Lab Performance

The earliest prototype was tested in the lab for the purpose of exploring and validating the velocimetry aspect of the instrument concept. For expediency, no means for converting the round input beam shape to a narrow rectangle was employed. Consequently, most photons were lost at the slit, so bright sources were used for the experiments. Using sunlight, the diurnal acceleration of the Earth was clearly shown in our measurements, and velocity fluctuations of a few meters per second similar in character to the known 5 minute oscillations of the photosphere were also seen in the data. The solar spectra were further monitored over a 1 month period. After diurnal and annual motion velocity components of the Earth have been deducted, the residual velocity component is consistent with the Earth's motion, which has an amplitude of 12 m s^{-1} caused by the Moon. This showed that the long-term drift over 1 month was not more than a few meters per second (see Erskine & Ge 2002 for details).

In order to fully understand instrument noise and long-term stability, a bromine absorption cell was used as a lab quiet and zero-velocity source instead of sunlight in later experiments. Like the iodine spectrum, the bromine spectrum has many absorption features in the green-wavelength region of interest. It is sufficiently different, however, to be distinguishable from the iodine spectrum. Therefore, the relative shift between the moiré fringe phase of bromine and iodine measured by the instrument can be used for testing zero-velocity repeatability and instrument noise. White light from an incandescent lamp passed through both the bromine and iodine vapor cells. The grating operated in the second diffraction order. The slit was

sufficiently narrow to partially resolve the continuum interferometer spectral comb, which had fringe visibility of 13%. In comparison, the Hg lamp produced a 45% visibility in five fringes along ~80 pixels in the slit direction and a 5.5 pixel (0.27 Å) FWHM peak in the dispersion direction, corresponding to $R \approx 20,000$ at 5400 Å.

Exposures were made every 15 s while phase stepping over a period of about 18 minutes and grouped into quadsets to produce 18 sets of velocity data. The fifth datum was assigned to be the master *StarId* and hence defined zero velocity. All other data, including sessions taken several days later, are referred to this master *StarId*.

Figure 5 shows the measurement results. During the first 18 minutes, the apparent velocity was measured with a repeatability of 0.76 m s^{-1}. This value includes both instrument and photon noise, but our Monte Carlo calculations show that the value was dominated by photon noise. Hence, the short-term instrument noise could be much less than 0.76 m s^{-1}.

This result demonstrates that it is possible to break the 1 m s^{-1} precision barrier with this new kind of inexpensive instrument. The spectral resolution of this instrument, $R \approx 20,000$, is about 3 times lower than that used in conventional Doppler spectrometers, $R \approx 60,000$ (e.g., Butler et al. 1996; Vogt et al. 2000). This is accomplished through the effect of heterodyning in our approach, which provides a simple and well-defined instrument response and also a factor of ~5 times magnification of the Doppler radial shift signal in the moiré fringes.

The repeatability of these measurements over longer terms has also been tested with the same setup. The second and third data sessions of Figure 5 were taken after 3 hr and again after 11 days, using the same *Star* and *Id* templates and master *StarId* of the first session. The results show long-term drifts of not more than 4 m s^{-1}, and the drift after 11 days was ~1 m s^{-1}. This precision and stability, even without further improvement, is comparable to the best performance with the echelle spectrometers (Butler et al. 1996; Vogt et al. 2000). Note that these measurements were made with an unstabilized-cavity apparatus without any environmental controls, constructed of breadboarded optics in the open air. The addition of simple environmental controls can be expected to improve the long-term stability.

3.2. Performance at the Lick 1 m

In 1999 December, a fiber-fed version of the prototype was coupled to the Lick 1 m telescope over a 10 night engineering run for initial starlight testing. Five bright nearby late-type stars were observed. These included α Persei ($V = 1.8$, F5 Iab), Capella ($V = 0.08$, G5 III), Procyon ($V = 0.34$, F5 IV), α Orionis ($V = 0.58$, M I), and Arcturus ($V = -0.04$, K1.5 III variable). The fringe data from Arcturus have the best quality in terms of fringe visibility and S/N. We took a total of 28 frames on Arcturus on 1999 December 22 with 5 minutes exposure per frame. The typical S/N is ~100 pixel^{-1}. The first six stellar frames without iodine were taken for creating star templates. Two additional frames were taken with one of interferometer arms blocked for correcting slant in absorption lines and flat-fielding the template frames. The following 15 frames were taken with iodine inserted in the beam. After this, five additional frames were taken with one of the interferometer arms blocked for flat-fielding the star plus iodine data. Figure 6a shows 800 pixels (out of 2500) of the raw fringing spectrum observed from Arcturus. The 2500 pixels cover 340 Å. Faint vertical moiré fringes can be seen, with about 3–4 fringe periods across the spectrum width. The humplike transverse profile of the spectrum may make the few percent contrast fringes difficult to discern in the photograph. The fringe visibility was consistent with that of the solar spectrum taken with the same instrument configuration during the day.

Figure 6b shows the fringes of Figure 6a after data reduction, essentially after the image has been flattened and all nonfringing components in the transverse direction removed. This shows a coherently averaged vector spectrum, called a whirl, representing the amplitude and phase of a fringing spectrum, obtained after initial data processing. In this pseudofringe method of displaying vector spectra, the vector magnitude and angle for each wavelength channel is represented by a synthetic fringe in a two-dimensional intensity map having corresponding amplitude and phase and fixed periodicity of 32 pixels unrelated to the actual periodicity. The whirl depicted here was used as the *Star* template. Figures 6c and 6d show *Id* and *StarId* whirls. Note that *StarId* appears consistent with being a vector sum of *Star* and *Id*, as presumed in the data analysis. The underlying interferometer sinusoidal comb is not seen here because it has been optically filtered away by the blurring action of the spectrograph, which was configured to have lower resolution than when used in lab tests.

Figure 7 plots the change in Doppler velocity versus time measured for Arcturus over a 55 minute session. The first datum was arbitrarily assigned zero velocity, and the diurnal acceleration of the Earth has been removed from the data. The RV varies with time with an amplitude of ~30 m s^{-1} during the observation. A further experiment using a bromine absorption cell was conducted during the daytime with the instrument set in the same configuration as that for observing Arcturus to measure the Doppler sensitivity. No temperature control was used for the bromine cell. Figure 8 shows the apparent velocity of the bromine spectrum relative to iodine, taken in two sessions over about 70 minutes. The datum at about 7:51 P.M. defines zero velocity. The repeatability is about ~5 m s^{-1} over the first ~30 minutes. The zero velocity appears to drift ~5 m s^{-1} over a period of an hour. This may be caused by the temperature fluctuations of the bromine cell during the observations. The overall rms precision is ~7 m s^{-1}. This measurement indicates that the large velocity variation component in the Arcturus data appears to be real. This RV variation seems consistent with previous measurements by an echelle spectrograph at the McDonald Observatory (Hatzes & Cochran 1993, 1994). In these previous observations, Hatzes & Cochran found that
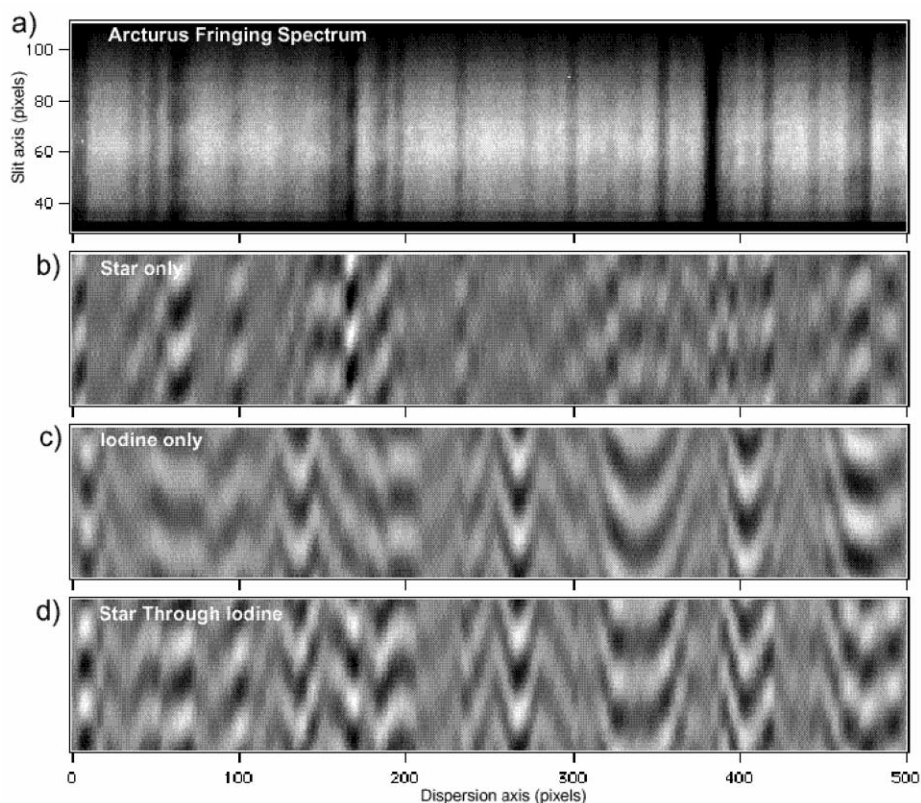
Fɪɢ. 6.—(*a*) Stellar moiré fringes of nearby star, Arcturus, taken by the fiber-fed EDI in 1999 December. (*b*), (*c*), and (*d*) are the fringing spectra after the nonfringing components have been removed during the data reduction process, for (*b*) the star alone, (*c*) iodine cell alone with a tungsten lamp, and (*d*) the star through the iodine cell. The underlying interferometer sinusoidal comb has been optically filtered away by the blurring action of the spectrograph, which was configured to have lower resolution than when used in lab tests.

Arcturus exhibited RV variations within a night as large as $\sim$100 m s^{-1}. These velocity variations may be associated with short-term (2.46, 4.03, and 8.5 day periods) radial pulsations of the star. Our RV variation component may be just a part of a larger variation shown in their measurements over a longer period.

4. DISCUSSION

Externally dispersed interferometry is a new approach for precision Doppler RV measurements. It provides a simple and well-defined instrument response function compared to the conventional echelle approach, resulting in lower instrument noise. The moiré fringe technique in practice allows 5–10 times magnification of the Doppler RV signal in the spectral dispersion direction of the grating spectrometer used in the dispersed interferometer. This enables a spectrometer with 5–10 times less resolving power (e.g., $R \sim 6000$–20,000) than current echelle spectrometers ($R \sim 60,000$) to achieve similar or better instrument sensitivity ($\sim$1 m s^{-1}) for measuring Doppler shifts in the spectral lines. The moderate spectral resolution requirement in this new instrument allows reduction in the instrument volume and mass by orders of magnitude, leading to much lower instrument cost. It also allows higher throughput design of the

instrument than the echelle spectrometer and also probably allows more rigid mechanical design of the instrument than the larger sized echelle spectrometers as a result of its compactness. This should lead to less long-term drift caused by instrument mechanical and thermal changes.

The experiments of the prototype dispersed interferometer at LLNL and the Lick 1 m telescope demonstrate some of the promising features of this new instrument concept: sensitivity,
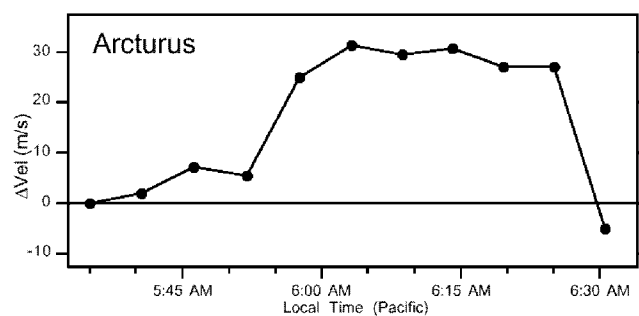

Fɪɢ. 7.—Arcturus Doppler velocity vs. time. The diurnal motion component caused by the Earth's rotation has been subtracted.
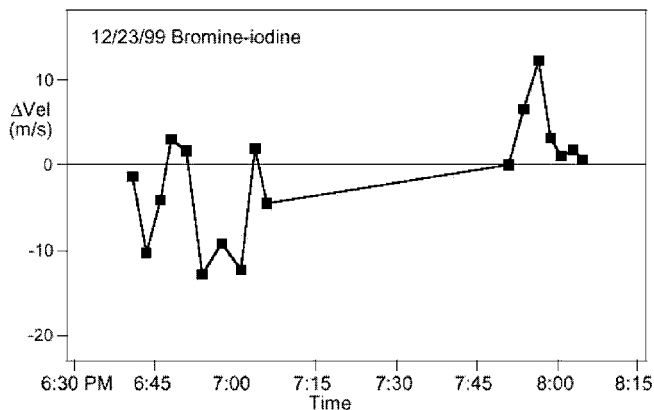
FIG. 8.—Zero-velocity repeatability by the fiber-fed EDI at the Lick 1 m telescope during the 1999 December run. Bromine absorption is used to simulate a zero-velocity Doppler source for the measurement. The disperser resolution $R = 5600$.

TABLE 1
TRANSMISSION FACTORS FOR THE DISPERSED INTERFEROMETER
SYSTEM AT THE LICK 1 m

Name	Measured Transmission (%)	Achievable Transmission (%)
Telescope transmission	70 (estimate)	70
Fiber feed system[a]	29	70
Interferometer system[b] (2 mirrors, 2 lenses, 1 BS, 1 delay plate)	31	80
Spectrograph (2 mirrors, 1 grating) and slit loss	18	37
CCD detector	67	90
Iodine cell	65	65
Total efficiency	0.5	9

[a] Our input fiber collects 3″.6 stellar beams. Photon loss due to seeing variation under typical seeing conditions (1″) is negligible; the major fiber-feed losses are due to focal ratio degradation, fiber transmission, and fiber-coupler optics transmission.

[b] A Mach-Zehnder type interferometer with two arms feeding is assumed.

compactness, and cost, and to some extent high throughput and stability. However, further experiments are necessary to explore the potential of the throughput and stability.

4.1. Doppler Sensitivity

Our prototype instrument has demonstrated ~ 1 m s^{-1} precision at $R \sim 20,000$ and S/N ~ 200 pixel^{-1}, which is a factor of 2–3 times better than the best detection sensitivity (~ 3 m s^{-1}) provided by echelle spectrometers with $R \sim 60,000$ and S/N ~ 200 pixel^{-1} (Butler et al. 1996; Vogt et al. 2000). In our case, the Doppler error is dominated by photon noise, while in the echelle, the instrument noise (~ 2 m s^{-1}) is the major contributor. In the echelle approach, especially with an iodine calibration reference, it may be challenging to push the Doppler precision beyond ~ 2 m s^{-1} unless the instrument response profiles can be better modeled to reduce the instrument noise. Other approaches with an echelle spectrometer, such as HARPS with the ESO 3.6 m telescope using a double fiber scrambler, higher echelle spectral resolution ($R \sim 90,000$), and thorium-argon calibration lamp and vacuum enclosure, have been proposed to reach 1 m s^{-1} precision (Pepe et al. 2000), but this needs to be proved. In our approach, higher Doppler sensitivity (<0.5 m s^{-1}) can be potentially achieved by simply increasing S/N for each detector pixel. We plan to verify this through further experiments.

The Doppler precision at the Lick 1 m telescope is ~ 7 m s^{-1}, a factor of ~ 7 times worse than the lab performance. Two major effects have prevented us from reaching ~ 1 m s^{-1} precision with our prototype instrument in the stellar observations: a factor of 3.6 times lower spectral resolution and reduced fringe visibility by a factor of 2.5 times. The lower spectral resolution blurred the moiré fringes and prevented resolution of the continuum spectral comb. The former effect reduced the moiré fringe visibility, and the latter increased the susceptibility

of the phase-stepping algorithms to noise. The blurring of the interferometer comb reduced the robustness to photon noise and increased the error by a similar factor, ~ 3.6 times. The reduced visibility increases the Doppler error proportionally by a factor of 2.5 times. Together, the two major effects lead to the larger error shown in the Lick data.

4.2. Compactness and Cost

Our new instrument approach has significantly reduced the planet-hunting instrument size and cost. The total hardware cost of our prototype is in the range of \$100,000. The size of the instrument is about 1.5 m × 1.0 m × 0.5 m. For comparison, high-resolution echelle spectrometers are usually multimillion dollar instruments; e.g., the Keck 10 m telescope HIRES costs more than \$4 million because of its huge size requirement for high resolution (~ 5.5 m × 4.9 m × 4 m; Vogt et al. 1994). The smaller optics used in our instrument allow the instrument design to be much more compact and cost much less. In the future, the total cost for an optimized dispersed interferometer including a high quantum efficiency (QE) 2K × 2K CCD, image slicer, high-quality optics coatings, etc., will probably still cost less than \$500,000. Cost effectiveness is therefore a significant advantage with this new instrument design.

4.3. Throughput

The total throughput of the interferometer system at the Lick 1 m telescope was measured to be about 0.5%, which includes the photon loss from the telescope, fiber feeding system, interferometer, spectrograph, and detector. The budget of transmission loss in each optical element is listed in Table 1. The major losses come from the fiber feed, interferometer, spectrometer entrance slit, and grating. The system was made from off-the-shelf optical components for rapid demonstration of the

concept and was not designed for high throughput. However, by simply optimizing the whole instrument component transmission and increasing the CCD detector QE (90% instead of the current 67%), an order-of-magnitude increase in total throughput is achievable as demonstrated in Table 1. The optimization includes substituting more light-efficient components such as antireflection-coated lenses (>98% transmission per surface) and protected silver-coated mirrors (>98% reflectivity at ~5400 Å), eliminating unnecessary surfaces, and implementing a higher efficiency fiber-feeding system (~70% vs. the measured ~29%) and spectrograph (a protected silver-coated first-order grating with ~65% efficiency and protected silver-coated mirrors). These together can bring the total efficiency to ~4.5%, a factor of 9 times improvement over the prototype. If both interferometer outputs are fed into the spectrometer with a new design (such as a Mach-Zehnder type interferometer), replacing the single-output feeding in the prototype (the Michelson type), the total efficiency will be doubled to ~9%. Based on this 9% efficiency, even if we do not improve Doppler radial velocity precision beyond ~7 m s^{-1}, the instrument can already compete with current planet-hunting echelle spectrometers (e.g., we can reach ~7 m s^{-1} Doppler precision for a $V = 3.9$ mag star in a 10 minute exposure with a 1 m aperture size telescope or a $V = 8.9$ mag in the same exposure with a 10 m telescope; the current Keck 10 m HIRES can reach ~3 m s^{-1} for $V = 8$ mag in a typical 10 minute exposure; Vogt et al. 2000).

Further improvement in throughput is possible by replacing the cylindrical lens and the current surface relief grating with an advanced image slicer and a volume phase holographic grating, respectively. Unlike the cylindrical lens, the image slicer slices the incoming beam and rearranges the slices along the slit direction to better match with the rectangular shape of the spectrograph entrance slit. The cylindrical lens we used at the Lick creates a 140×2000 μm rectangular image on the slit. About 60% of the photons can pass through the 84 μm wide spectrograph entrance slit. For an image slicer, 80% transmission has been reported (Content 2000). The best available volume phase holographic gratings can provide more than 90% grating efficiency for unpolarized light (Barden et al. 2000). If these new instrument components are employed in our instrument, the total throughput can be increased to ~85%. For the same exposure time, we can push 2 mag fainter. Therefore, once the new instrument is fully functional, it will have the potential to reach more than 2.5 mag fainter than an echelle spectrometer at the same size telescope.

4.4. Stability

Our prototype demonstrates that the instrument stability over a couple of weeks is at the level of ~4–8 m s^{-1}, larger than the instrument instantaneous sensitivity level ~1 m s^{-1}. This kind of stability is reasonably good given that no efforts were made in the prototype to minimize velocity drifts. For com-

parison, all the planet-hunting echelle spectrometers were operated in temperature-controlled rooms. Several factors such as the unregulated temperature and pressure of the bromine calibration cell and the unstabilized interferometer cavity may have contributed to the zero-velocity drift. Without the interferometer cavity stabilization scheme, a drift of the interferometer as much as one fringe over 2 minutes has been observed. In addition, the interferometer drift in transverse fringe spacing due to mirror tilt may also have contributed to this drift. This is because all these change fringe visibilities of the iodine and bromine absorption lines differently. Because of the vector nature of fringe data, the differential change in visibility between iodine and bromine is likely to lead to zero-velocity drift. Further experiments are necessary to investigate the exact cause for the instrument long-term drifts.

4.5. Calibration References

In our approach, we chose the iodine as a reference because it can be easily made and has been widely accepted as a standard reference. However, it can be replaced by other reference sources. As mentioned earlier, the instrument response of the dispersed interferometer is a well-defined and stable truncated sinusoidal function. The reference spectra are therefore only needed for measuring the moiré fringe phase zero point, not for measuring instrument response at different wavelengths as in the echelle approach (Valenti et al. 1995; Butler et al. 1996). For a Doppler precision of ~1 m s^{-1}, a reference with ~100 absorption lines is necessary. For comparison, the echelle approach requires iodine to provide thousands of lines for calibrating instrument responses. Therefore, this instrument allows potential use of other reference sources with fewer absorption or emission lines than iodine. This in turn makes the interferometer more applicable in wave bands other than the current green iodine absorption wavelengths, such as near-IR wavelengths.

4.6. Potential Applications

The improved throughput of the new instrument will allow us to search for planets around fainter field stars than current survey limits and also to search for planets associated with stars in different-aged clusters. More planets found with new high-throughput instruments will help to determine not only the fundamental physical processes underlying planetary formation but also the proper statistical distribution of orbital elements, planetary masses, frequency (especially among different age stars), planet/star property correlations such as metallicity, and the characterization of multiple-planet systems.

The potential application of this instrument in the near-IR will open up new possibilities for efficient searches for planets around M dwarfs, which have ~10 times more photon flux in the near-IR than in the visible (Kirkpatrick et al. 1993). Furthermore, M dwarfs are dominant in the solar neighborhood, constituting ~80% of nearby ($d < 8$ pc) stars (Henry 1991). Current echelle Doppler searches have covered F, G, and K

stars that are relatively bright in the visible. M dwarfs, however, have for the most part not been covered as they are too faint ($V \sim 11$–13 mag; Henry, Kirkpatrick, & Simons 1994) to be efficiently observed. Even at the largest telescopes such as the Keck 10 m, only very nearby M stars such as Gliese 876 ($V = 10.17$, $I = 6.76$, $J = 5.97$, $d = 4.7$ pc; Marcy et al. 1998; Delfosse et al. 1998) have been observed. Therefore, there is a strong need for developing new instruments capable of searching for planets around M dwarfs in the near-IR wavelengths.

The new moiré approach also has the potential for planet searches around early-type stars and white dwarfs that have very broad stellar absorption features and have been totally neglected by current echelle techniques. Once the interferometer comb period matches the broad absorption line width, the moiré fringes should allow us to precisely determine the Doppler RV signal. Hence, this new instrument can potentially significantly improve the precision of radial velocity measurements of early-type stars. This new technique also opens the possibility of using multiple fibers to simultaneously monitor RV variations from binary stars, multiple stars, or stars in star clusters, taking advantage of the simple one dispersion order operation.

REFERENCES

Barden, S. C., Arns, J. A., Colburn, W. S., & Williams, J. B. 2000, PASP, 112, 809

Barker, L. M., & Schuler, K. W. 1974, J. Appl. Phys., 45, 3692

Butler, R. P., Marcy, G. W., Williams, E., McCarthy, C., Dosanjh, P., & Vogt, S. 1996, PASP, 108, 500

Cochran, W. D., Hatzes, A. P., Butler, R. P., & Marcy, G. W. 1997, ApJ, 483, 457

Connes, P. 1985, Ap&SS, 110, 211

Content, R. 2000, in ASP Conf. Ser. 195, Imaging the Universe in Three Dimensions: Astrophysics with Advanced Multi-Wavelength Imaging Devices, ed. W. van Breugel & J. Bland-Hawthorn (San Francisco: ASP), 518

Delfosse, X., Forveille, T., Mayor, M., Perrier, C., Naef, D., & Queloz, D. 1998, A&A, 338, L67

Douglas, N. G. 1997, PASP, 109, 151

Erskine, D. J. 2001, US Patent 6,115,121

Erskine, D. J., & Ge, J. 2000, in ASP Conf. Ser. 195, Imaging the Universe in Three Dimensions: Astrophysics with Advanced Multi-Wavelength Imaging Devices, ed. W. van Breugel & J. Bland-Hawthorn (San Francisco: ASP), 501

———. 2002, PASP, submitted

Fischer, D. A., Marcy, G. W., Butler, R. P., Vogt, S. S., Frink, S., & Apps, K. 2001, ApJ, 551, 1107

Frandsen, S., Douglas, N. G., & Butcher, H. R. 1993, A&A, 279, 310

Harvey, J., et al. 1995, in ASP Conf. Ser. 76, Gong '94: Helio- and Astero-Seismology from the Earth and Space, ed. R. K. Ulrich, E. J. Rhodes, Jr., & W. Däppen (San Francisco: ASP), 432

Hatzes, A. P., & Cochran, W. D. 1993, ApJ, 413, 339

———. 1994, ApJ, 422, 366

Henry, T. J. 1991, Ph.D. dissertation, Univ. Arizona

Henry, T. J., Kirkpatrick, J. D., & Simons, D. A. 1994, AJ, 108, 1437

Hilliard, R. L., & Shepherd, G. G. 1966, J. Opt. Soc. Am., 56, 362

Kirkpatrick, J. D., Kelly, D. M., Rieke, G. H., Liebert, J., Allard, F., & Wehrse, R. 1993, ApJ, 402, 643

Kozhevatov, I. E., Kulikova, E. Kh., & Cheragin, N. P. 1995, Astron. Lett., 21, 418

———. 1996, Sol. Phys., 168, 251

Lin, D. N. C., Bodenheimer, P., & Richardson, D. C. 1996, Nature, 380, 606

Marcy, G. W., & Butler, R. P. 1996, ApJ, 464, L147

———. 1998, ARA&A, 36, 57

Marcy, G. W., Butler, R. P., & Vogt, S. S. 2000, ApJ, 536, L43

Marcy, G. W., Butler, R. P., Vogt, S. S., Fischer, D., & Lissauer, J. J. 1998, ApJ, 505, L147

Marcy, G. W., Cochran, W. D., & Mayor, M. 2000, in Protostars and Planets IV, ed. V. Mannings, A. P. Boss, & S. S. Russell (Tucson: Univ. Arizona Press), 1285

Mayor, M., Naef, D., Pepe, F., Queloz, D., Santos, N., Udry, S., & Burnet, M. 2000, in IAU Symp. 202, Planetary Systems in the Universe: Observation, Formation, and Evolution, ed. A. Penny, P. Artymowicz, A.-M. Lagrange, & S. Russel (ASP Conf. Ser.; San Francisco: ASP)

Mayor, M., & Queloz, D. 1995, Nature, 378, 355

Noyes, R. W., et al. 1997, ApJ, 483, 111

Pepe, F., et al. 2000, Proc. SPIE, 4008, 582

Saar, S. H., Butler, R. P., & Marcy, G. W. 1998, ApJ, 498, L153

Saar, S. H., & Fischer, D. 2000, ApJ, 534, L105

Title, A. M., & Ramsey, H. E. 1980, Appl. Opt., 19, 2046

Valenti, J., Butler, R. P., & Marcy, G. W. 1995, PASP, 107, 966

Vogt, S. S., Marcy, G. W., Butler, R. P., & Apps, K. 2000, ApJ, 536, 902

Vogt, S. S., et al. 1994, Proc. SPIE, 2198, 362